photonics

MDPI

Article

Improved Shielding Effectiveness Model for Honeycomb Waveguide in Laser Controller Enclosures

Shaoqian Zhang [1,2], Yuanxin Huang [1,2], Wei He [1,2], Pei Xiao [3], Zhaoxuan Tang [3] and Fuwei Li [1,2,4,*]

[1] Changsha Institute of Mining Research Co., Ltd., Changsha 410012, China; 19113167414@163.com (S.Z.); hyx8875@126.com (Y.H.); jane.eary@163.com (W.H.)
[2] State Key Laboratory of Safety Technology of Metal Mines, Changsha 410012, China
[3] College of Electrical and Information Engineering, Hunan University, Changsha 410082, China; xiaopei@hnu.edu.cn (P.X.); tzx234@hnu.edu.cn (Z.T.)
[4] Minmetals National Innovation Center Technology (Hunan) Co., Ltd., Changsha 410082, China
* Correspondence: 18974939931@163.com

Abstract

Electromagnetic leakage through ventilation interfaces is a critical challenge in photonic instrumentation, where laser controllers and photoelectric readout circuits are highly sensitive to external interference. In photonic instruments, enclosure leakage may couple into laser controller and photoelectric readout circuits, degrading optical signal stability and electromagnetic cleanliness. To enable fast shielding assessment at the packaging stage, this paper proposes an improved semi-analytical shielding-effectiveness model for hexagonal honeycomb waveguides used in laser controller enclosures. Within a transmission matrix formulation, finite-conductivity loss is included through propagation constant correction, and inter-cell interaction is represented by an array-based coupling correction. The model captures high-frequency additional transmission effects that are not reflected in simplified independent-cell formulations. Validation against CST full-wave simulations from 1 to 40 GHz demonstrates improved agreement, particularly near cutoff and in the upper-frequency range, with substantially lower computational cost than full-wave optimization loops. Geometry-dependent trends are further quantified to support EMC co-design of ventilation and enclosure structures in photonic and optoelectronic platforms.

Keywords: laser controller enclosure; honeycomb waveguide; shielding effectiveness; mutual coupling correction; electromagnetic compatibility

1. Introduction

Photonic systems such as laser ranging instruments, electro-optical tracking units, and optical communication terminals increasingly integrate high-density control electronics within compact enclosures. As power density rises, ventilation openings become necessary for thermal management; however, these openings also form dominant electromagnetic leakage paths that can degrade laser controller stability, increase readout noise, and reduce overall EMC robustness. Honeycomb vent waveguides are widely adopted in such enclosures because they provide airflow while preserving shielding capability. Therefore, accurate and efficient shielding-effectiveness modeling of honeycomb structures is essential for packaging-level EMC design in photonic equipment [1,2]. In these platforms, honeycomb ventilation waveguides are widely adopted because they provide high airflow open-area ratios while retaining waveguide-below-cutoff shielding capability [3,4]. Particularly in optical equipment with strict electromagnetic cleanliness requirements,

Check for updates

Received: 27 March 2026
Revised: 10 April 2026
Accepted: 11 April 2026
Published: 14 April 2026

Copyright: © 2026 by the authors. Licensee MDPI, Basel, Switzerland. This article is an open access article distributed under the terms and conditions of the Creative Commons Attribution (CC BY) license.

ventilation-window performance directly affects detector stability, low-noise analog front ends, high-speed optoelectronic interfaces, and overall EMC margins. In millimeter-wave and 5G-relevant bands, ventilation windows can no longer be treated as simple electromagnetic barriers; their response is strongly geometry- and array-dependent, and even small design deviations may propagate to system-level EMC test failure risks [5]. Therefore, for optical and optoelectronic enclosures, a wideband and accurate shielding-effectiveness prediction model is of high practical importance.

Although classical Schelkunoff transmission theory provides the foundation for shielding analysis, its direct application to modern dense honeycomb arrays at high frequencies is often limited in accuracy [6–8]. Many conventional analytical models are built on an isolated-aperture assumption, where total leakage is approximated as a scalar superposition of single-aperture leakage. For high-density aperture arrays commonly used in compact optical equipment, this approximation may underrepresent inter-aperture mutual coupling; adjacent cells can act as secondary reradiating sources and produce coherent near-field interactions [9–11]. At high frequencies, such interactions may introduce additional effective transmission paths, resulting in discrepancies between predicted and measured SE [12–15].

In addition, conventional formulations frequently idealize waveguide walls as perfect electric conductors (PEC), which does not fully reflect practical enclosure materials such as aluminum alloys and steel [14,16]. Their finite conductivity leads to frequency-dependent ohmic dissipation under skin-effect conditions. Moreover, approaches based mainly on real-valued attenuation constants often neglect phase evolution, reducing their capability to capture thickness-related resonant behavior [17].

To address these limitations while avoiding the high computational cost of full-wave multiscale simulation, this work develops an improved semi-analytical model based on the transmission matrix method [18], with explicit corrections for finite-conductivity loss and inter-aperture coupling, targeting practical SE prediction for ventilated optical and optoelectronic enclosures.

2. Improved Theoretical Model

To overcome the limitations of traditional cutoff waveguide theory, this paper establishes an improved transmission matrix model based on microwave network theory [19]. This chapter first introduces the general calculation framework of the improved model, followed by a detailed derivation of its two core correction terms: the propagation constant correction based on material properties and the mutual coupling factor correction based on array theory.

2.1. General Framework Based on Transmission Matrix Method

Considering the physical process of electromagnetic waves incident on a honeycomb ventilation window as shown in Figure 1, it can be modeled as a three-layer cascaded medium: "Free Space (I)—Honeycomb Waveguide (II)—Free Space (III)."

Since honeycomb structures typically operate below the cutoff frequency and the primary concern is TE mode leakage, the transmission equations for the tangential electric field E and magnetic field H are established using two-port network theory. According to the transmission matrix method, the total transmission matrix Ttotal describes the mapping relationship between the input field intensity (E_{in},H_{in}) and the output field intensity (E_{out},H_{out}):

$$\begin{vmatrix} E_{in} \\ H_{in} \end{vmatrix} = |T_{total}| \begin{vmatrix} E_{out} \\ H_{out} \end{vmatrix} = |T_{in}||T_{waveguide}||T_{out}| \begin{vmatrix} E_{out} \\ H_{out} \end{vmatrix} = \begin{vmatrix} A & B \\ C & D \end{vmatrix} \begin{vmatrix} E_{out} \\ H_{out} \end{vmatrix} \quad (1)$$

where T_{in} and T_{out} represent the transmission and reflection matrices at the air/waveguide interfaces, and $T_{waveguide}$ represents the transmission matrix within the waveguide. To facilitate the subsequent comparison of improvement effects, the basic parameters based on traditional cutoff waveguide theory are first defined:

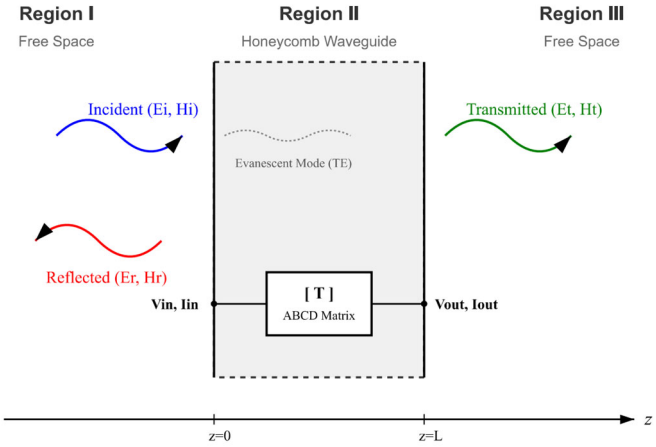


Figure 1. The process of electromagnetic waves incident on the honeycomb waveguide.

Free Space Wave Impedance (Z_0): Regions I and III are air media, and their wave impedance is a constant:

$$Z_0 = \sqrt{\frac{\mu_0}{\varepsilon_0}} \approx 377\ \Omega \tag{2}$$

Honeycomb Waveguide Characteristic Impedance (Z_c): Region II is a hexagonal metal waveguide. For the TE mode, its equivalent wave impedance Z_c depends on the relationship between the frequency and the cutoff frequency:

$$Z_c = \frac{j\omega\mu}{\gamma} = \frac{Z_0}{\sqrt{1-\left(\frac{f_c}{f}\right)^2}} \tag{3}$$

where the cutoff frequency is $f_c = \frac{c}{2\sqrt{3}a}$, c is the speed of light, and a is the side length of the hexagonal waveguide.

In the total transmission matrix $|T_{total}|$, the matrix elements A, B, C, D are the core parameters determining the system's transmission characteristics:

$$\begin{cases} A = cosh(\gamma L) \\ B = Z_c sinh(\gamma L) \\ C = \frac{1}{Z_c} sinh(\gamma L) \\ D = cosh(\gamma L) \end{cases} \tag{4}$$

where L is the waveguide length. The final shielding effectiveness depends on the transmission coefficient T of the total grid:

$$T = \frac{2}{A + \frac{B}{Z_0} + CZ_0 + D} \tag{5}$$

Traditional calculation methods obtain shielding effectiveness by substituting ideal parameters into the above formula to calculate $SE = 20\log_{10}\frac{1}{|T|}$. However, this method ignores pore wall losses and inter-pore coupling. The improvement in this study lies in correcting the propagation constant γ and the coupling correction term in the above formulas to better align with physical reality.

2.2. Key Parameter Corrections

2.2.1. Propagation Constant Correction

In traditional cutoff waveguide theory, the propagation constant γ is usually regarded as a purely real number, which only depends on the geometric attenuation of the waveguide. However, this assumption premises that the waveguide walls are ideal electrical conductors ($\sigma \to \infty$). In reality, commercial honeycomb panels are usually made of aluminum or steel, which have finite conductivity.

To correct this defect, this model introduces a complex propagation constant γ_{new}. based on material properties. Its correction process involves the derivation of the following two physical dimensions:

When electromagnetic waves impinge upon a non-ideal metallic surface, the waves penetrate the metal to a certain depth (skin depth δ), generating ohmic losses. First, the surface impedance Z_s of the metal wall is defined:

$$Z_s = R_s + jX_s = (1+j)\sqrt{\frac{\pi f \mu}{\sigma}} \tag{6}$$

where f is the incident wave frequency, σ is the metal conductivity, μ is the permeability, and $\delta = \sqrt{\frac{2}{\omega\mu\sigma}}$ is the skin depth.

According to microwave perturbation theory, this finite surface impedance leads to an additional wall loss attenuation term (α_{wall}) on top of the traditional geometric attenuation constant (α_{geo}). For hexagonal waveguides, this correction term is derived as:

$$\alpha_{new} = \alpha_{geo} + \alpha_{wall} = \frac{2\pi}{c}\sqrt{f_c^2 - f^2} + \frac{K_{shape}R_s}{aZ_0\sqrt{1-\left(\frac{f}{f_c}\right)^2}} \tag{7}$$

where K_{shape} is the shape correction factor, which is approximately 0.8~0.9 for regular hexagonal holes [20].

In the traditional model, when the operating frequency is below the cutoff frequency, the phase constant β is generally regarded as 0. Nevertheless, in a lossy medium, wave propagation encompasses not only amplitude attenuation but also phase lag. Therefore, a phase constant that takes into account material properties is established:

$$\beta_{new} = \frac{\omega}{c} \times \left(1 + 0.5\left(\frac{a}{\lambda}\right)^2 \times k_{material}\right) \tag{8}$$

where $k_{material}$ is the material correction factor

$$k_{material} = Re\left(\frac{Z_s}{\eta_0}\right) \times k_{shape} \tag{9}$$

Combining the above two parts, the improved propagation constant is:

$$\gamma_{new} = \alpha_{new} + j\beta_{new} \tag{10}$$

2.2.2. Coupling Correction Term

In high-density arrays such as honeycomb waveguides, the equivalent impedance at the input interface is no longer determined solely by single-hole geometry but is also strongly interfered with by the radiation fields of adjacent apertures. The traditional model ignores this near-field coupling. Based on antenna array theory, this paper treats each aperture as a magnetic current dipole and introduces a coupling correction factor C_{MN} to quantify the electromagnetic interaction between pore arrays.

This coupling factor is defined as the ratio of the intensity of the induced field generated by the equivalent magnetic current source at the m-th aperture to the intensity of the excitation source at the n-th aperture. Specifically, when a plane wave impinges upon a multi-hole array, each hole is not only directly excited by the incident wave but also influenced by the superposition of secondary scattered fields generated by all the other holes. This can be computed by calculating the excitation exerted by the field of one hole on another:

$$C_{MN} = \frac{j\omega\mu}{4\pi}\frac{e^{-k_0 R_{mn}}}{R_{mn}}\left[1 + \frac{1}{jk_0 R_{mn}} - \frac{1}{(jk_0 R_{mn})^2}\right] \tag{11}$$

where R_{mn} represents the distance between the centers of two holes. Each aperture is regarded as an excited dipole, and the total leakage field represents the superposition of the coupling effects of all apertures. In the case of a hexagonal honeycomb structure, each aperture has six nearest-neighbor apertures (with a distance denoted as d) and six next-nearest-neighbor apertures (with a distance denoted as $\sqrt{3}d$). Consequently, the summation within the coupling correction term can be formulated as:

$$\sum_{m,n} |C_{MN}|^2 \approx N \times \left[6|C(d)|^2 + 6|C\left(\sqrt{3}d\right)|^2 + \cdots\right] \tag{12}$$

where N is the total number of holes.

Since inter-pore coupling decays rapidly with increasing distance, to simplify the calculation, the calculation is performed using the two most influential terms (nearest and next-nearest neighbors). Thus:

$$\sum_{m,n} |C_{MN}|^2 \approx N \times \left[6|C(d)|^2 + 6|C\left(\sqrt{3}d\right)|^2\right] \tag{13}$$

Finally the coupling correction term can be expressed as:

$$\Delta SE = 10log_{10}\left[1 + \sum |C_{MN}|^2\right] \tag{14}$$

In essence, this inter-cell coupling correction is conceptually derived as an asymptotic approximation rather than a strictly rigorous analytical solution. From a physical intuition perspective, this formulation captures the spatial overlapping of evanescent fields leaking from adjacent sub-wavelength apertures, where closely packed holes act as coupled parasitic radiators. While a completely rigorous mathematical treatment would require an infinite summation of mutual interactions across the entire periodic array, the rapid decay of near-field evanescent coupling with distance justifies truncating the interaction ranges. Consequently, limiting the summation to the nearest and next-nearest neighbors serves as an optimal semi-analytical compromise. This approach effectively captures the dominant physical mechanisms of near-field leakage overlapping while fulfilling the requirement for rapid macroscopic engineering prediction.

2.2.3. Solution of the Improved Model

Using the transmission matrix method and considering the boundary conditions of the three regions, the matrix equation can be listed as follows:

$$\begin{bmatrix} 1 & 1 & -1 & 0 \\ Z_C & -Z_C & 0 & \eta_0 \\ 0 & 0 & cosh(\gamma_{new}t) & sinh(\gamma_{new}t) \\ 0 & 0 & \frac{sinh(\gamma_{new}t)}{Z_C} & \frac{cosh(\gamma_{new}t)}{Z_C} \end{bmatrix} \begin{bmatrix} E_0 \\ R \\ A \\ B \end{bmatrix} = \begin{bmatrix} 0 \\ 0 \\ T \times E_0 \\ -\frac{T \times E_0}{\eta_0} \end{bmatrix} \tag{15}$$

where E_0 represents the incident wave amplitude (known, here set $E_0 = 1$), and Z_C represents the honeycomb pore characteristic impedance. For the TE mode, it can be stated as previously defined. η_0 represents the free space wave impedance, and R represents the reflection coefficient. A and B represent the cosine and sine term coefficients of the honeycomb panel's internal region. Solving the above matrix yields the transmission coefficient T:

$$T = \frac{2}{cosh(\gamma t) + 0.5 \times \left(\frac{Z_C}{\eta_0} + \frac{\eta_0}{Z_C}\right) sinh(\gamma t)} \tag{16}$$

Therefore, the modified shielding effectiveness is:

$$\boldsymbol{SE = 20log_{10}\left(\frac{1}{|T|}\right) + \Delta SE = 20log_{10}\left(\frac{1}{|T|}\right) + 10log_{10}\left[1 + \sum |C_{MN}|^2\right]} \tag{17}$$

3. Simulation Verification and Result Analysis

3.1. Simulation Setup

To assess the actual electromagnetic shielding performance of hexagonal honeycomb ventilation apertures and verify the predictive capacity of the analytical model, full—wave electromagnetic simulations were carried out using CST Microwave Studio. The unit cell structure is presented in Figure 2.

Parameters: a = 3 mm, L = 30 mm, and d = 3.5 mm. Considering that actual lossy conductors partially absorb energy, the material was defined as aluminum (σ = 3.775 × 107 S/m). The calculated cutoff frequency is approximately 31.86 GHz; therefore, the simulation frequency range was set to 1–40 GHz. The CST Microwave Studio Frequency Domain Solver was utilized for the full-wave simulation.

Boundary Conditions: Unit Cell periodic boundaries were applied in the X and Y directions, while Floquet ports were assigned in the Z direction. This setup is equivalent to simulating an infinite honeycomb array, enabling the complete capture of mutual coupling effects.

Codes for both the traditional model and the proposed new model were developed in MATLAB R2020b to calculate their respective values across the 1–40 GHz frequency range, followed by a comparative.

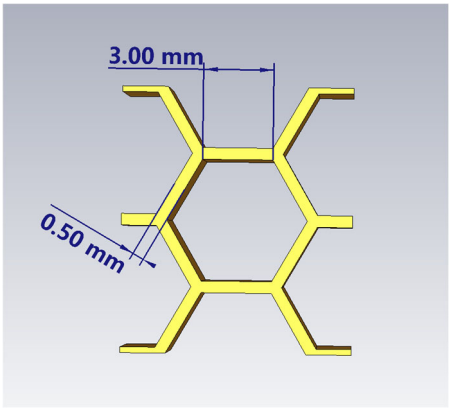


Figure 2. Unit cell model.

3.2. Comparison of Results and Discussion

Benchmarking with full-wave simulation and the conventional model reveals that the proposed model exhibits enhanced physical fidelity and practical prediction capabilities across frequency bands, which supports the electromagnetic compatibility (EMC)-oriented design of photonic laser controller enclosures.

Figure 3 presents a comparison of the shielding effectiveness results derived from the traditional analytical model, the new model proposed in this paper, and the CST full-wave simulation. The advantages of the new model and its underlying physical mechanisms are expounded upon below across diverse frequency bands.

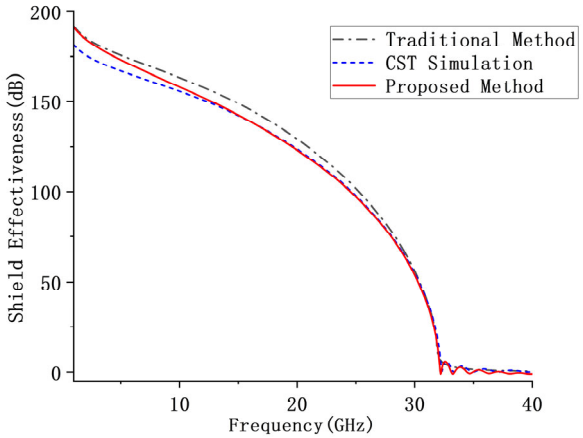


Figure 3. Comparison of shielding effectiveness.

The following phenomena can be observed from the results:

3.2.1. Low-Frequency Zone (1–10 GHz)

Within this frequency band, the waveguide exists in a profound cutoff state, and the shielding effectiveness values are remarkably high. Figure 4 shows a comparison of the three results in the low-frequency zone. Both the traditional model and the proposed model mirror the fundamental characteristic of the waveguide functioning as a high-pass filter. Nevertheless, even within the low-frequency band, the conductivity of actual aluminum metal walls is not infinite. By introducing surface impedance correction, the proposed model demonstrates trends that align more closely with physical reality compared to traditional models, which only account for geometric attenuation. These results validate the fundamental accuracy of the model at low frequencies far from the cutoff point.

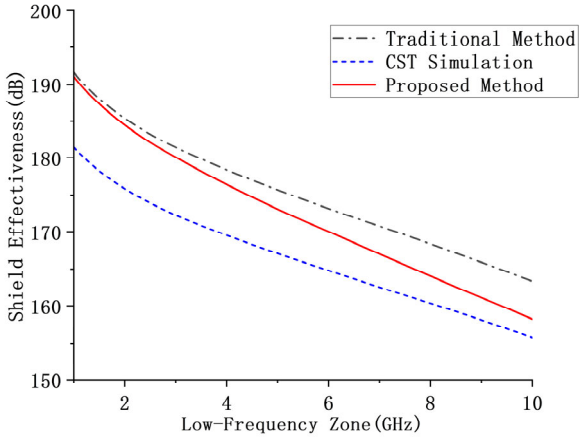


Figure 4. Comparison of shielding effectiveness in the low-frequency zone.

3.2.2. Mid-Frequency Zone (10–30 GHz)

This is the core operating region of the waveguide. Figure 5 shows a comparison of three results in the mid-frequency zone. As frequency increases, the shielding effectiveness shows a linear downward trend. The main error source in this frequency band is the array mutual coupling effect. Traditional models are based on Schelkunoff's single-aperture

theory, which neglects electromagnetic field interactions within densely packed honeycomb aperture arrays. According to array antenna theory, adjacent apertures behave like dipole arrays when excited, leading to superposition of their radiated fields. The new model introduces a "mutual coupling factor" that effectively characterizes this "virtual leakage channel" between neighboring holes, revealing how inter-hole coupling degrades shielding performance. This ensures the new model not only achieves higher accuracy but also provides more conservative and safer design margins compared to traditional formulas.

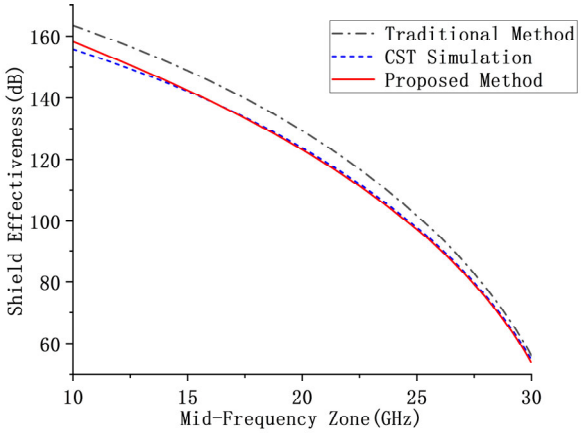


Figure 5. Comparison of shielding effectiveness in the mid-frequency zone.

3.2.3. High-Frequency/Cutoff Zone (30–40 GHz)

As $f \to f_c$, the wavelength of the electromagnetic wave shortens, the interference effects resulting from the phase difference between apertures are intensified. Figure 6 shows a comparison of three results in the high-frequency/cutoff zone. In this region, the influence of the mutual coupling correction term and the frequency-dependent surface impedance correction term within the improved model increases. This results in an accelerated decrease in the real part of the attenuation constant α. This demonstrates that the proposed model effectively captures the mechanism of enhanced energy transmission as the frequency approaches the cutoff limit.

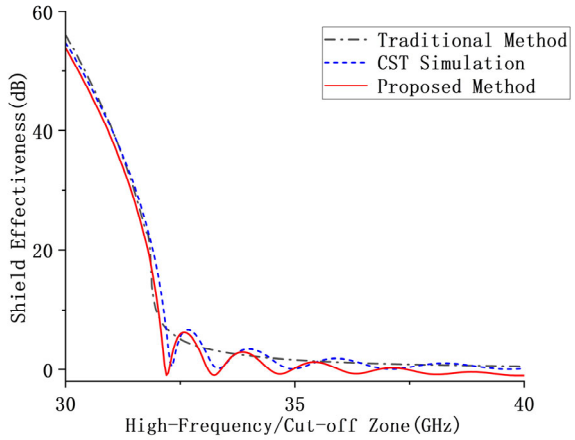


Figure 6. Comparison of shielding effectiveness in the high-frequency/cutoff zone.

In contrast to the traditional model, which solely depends on the linear extrapolation of geometric dimensions, the proposed model reflects high-frequency resonance effects more acutely and shows a steeper declining trend. Although it does not fully replicate the sharp decline in shielding effectiveness caused by resonance observed in full-wave simulations, its curve identifies the risk of high-frequency leakage at an earlier stage.

To substantiate the core claim of improved accuracy beyond visual curve comparison, closed-loop quantitative error analyses were conducted across different frequency zones. Table 1 summarizes the key quantitative metrics, including the Mean Absolute Error (MAE) and Maximum Deviation (MaxD), using the full-wave simulation (CST) results as the benchmark. For the traditional analytical model, the overall MAE reaches 7.91 dB, with pronounced errors in the low-frequency zone (MAE of 8.60 dB) and mid-frequency zone (MAE of 5.25 dB), reaching a maximum deviation (MaxD) of 10.17 dB. In contrast, the proposed improved model suppresses these errors across all bands, reducing the total MAE to merely 2.06 dB. Notably, in the mid-frequency zone, the proposed model achieves an exceptional fit with an MAE of just 0.73 dB and a MaxD of 2.46 dB (compared to the traditional model's 5.25 dB and 7.64 dB, respectively). Even near the high-frequency/cutoff zone, the proposed model maintains high predictive reliability with an MAE of 0.93 dB. These quantitative metrics demonstrate the enhanced reliability and robust fitting accuracy of the proposed model over the entire frequency spectrum.

Table 1. MAE and MaxD of both traditional and proposed methods.

Frequency Zone	Method	MAE (dB)	MaxD (dB)
Low-Frequency Zone	Traditional	8.60	10.17
	Proposed	5.76	9.6
Mid-Frequency Zone	Traditional	5.25	7.64
	Proposed	0.73	2.46
High-Frequency/Cutoff Zone	Traditional	1.37	7.09
	Proposed	0.93	6.63
Total	Traditional	7.91	10.17
	Proposed	2.06	9.6

4. Analysis of the Influence of Key Structural Parameters on Shielding Effectiveness

In the preceding chapter, the improved analytical model proposed in this work was comprehensively validated against full-wave electromagnetic simulations and the conventional Schelkunoff model across the full frequency band. Building on this validated framework, the present chapter quantitatively examines how key geometric parameters—particularly waveguide length and aperture size—influence the shielding effectiveness (SE) of hexagonal honeycomb vents. Using a controlled-variable approach, we clarify the distinct parameter-response mechanisms in the low-frequency cutoff region and the high-frequency resonance region. Furthermore, the model is applied to a representative laser controller enclosure to assess its engineering accuracy and error characteristics under realistic boundary and mounting conditions. These insights directly support rapid, physics-based shielding evaluation and optimization of photonic system enclosures during early-stage design.

4.1. Shielding Effectiveness Under Different Aperture Sizes

The waveguide side length a directly determines both the cutoff frequency f_c of the waveguide and the magnitude of its shielding effectiveness. Figure 7 illustrates the impact of different waveguide side lengths (a = 3 mm, 5 mm, 7 mm, 9 mm) on SE under the condition of a fixed length L = 30 mm.

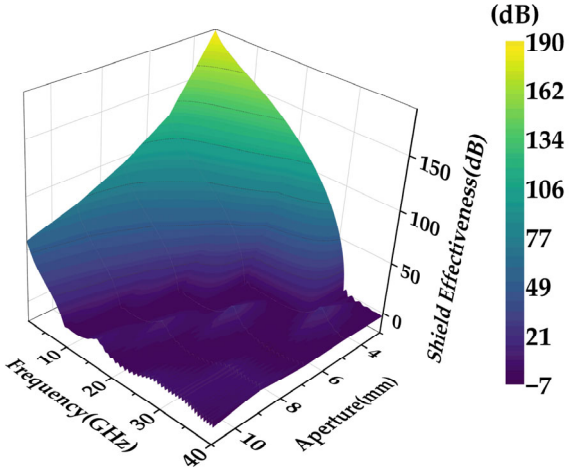


Figure 7. Shielding effectiveness under different aperture sizes.

The results indicate that increasing the aperture size shifts the cutoff frequency toward the lower frequency range. Larger apertures cause the waveguide to enter the transmission state earlier, which significantly reduces the effective shielding bandwidth in the medium-to-high frequency bands. At the same frequency, a larger aperture results in a smaller attenuation constant for single-mode transmission, leading to a downward shift of the overall shielding effectiveness curve. Therefore, under the premise of meeting ventilation and heat dissipation requirements, engineering designs should prioritize smaller apertures to achieve a wider shielding frequency band.

4.2. Shielding Effectiveness Under Different Waveguide Lengths

Waveguide length L serves as the core parameter determining the attenuation characteristics of a cutoff waveguide. Figure 8 illustrates the variation curves of shielding effectiveness (SE) under different waveguide lengths (L = 10–40 mm), given a fixed side length (D = 3 mm) and inter-hole spacing (s = 0.5 mm).

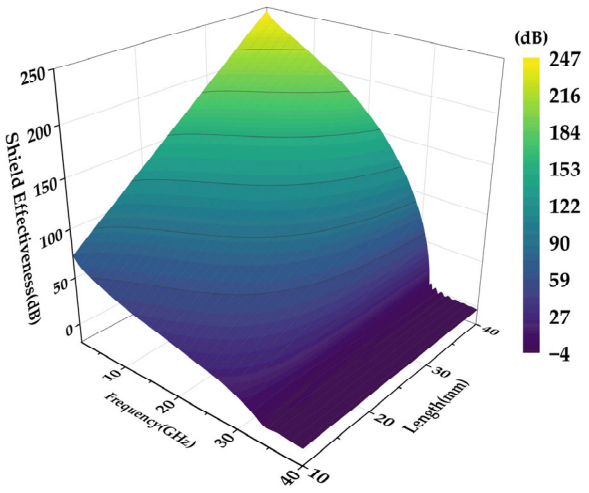


Figure 8. Shielding effectiveness under different waveguide lengths.

The results indicate that below the cutoff frequency ($f < f_c$), SE exhibits a linear growth trend as L increases. This is attributed to the dominance of the attenuation constant α in the cutoff waveguide mode, where the SE value is approximately proportional to αL. Consequently, increasing the thickness is the most direct and effective method for enhancing shielding performance in the low-frequency band.

However, when the frequency approaches or exceeds the cutoff frequency, the waveguide enters the transmission mode. In this regime, the attenuation gain provided by the thickness L diminishes rapidly, and the SE curves for different thicknesses tend to converge. This indicates that simply increasing the thickness cannot effectively address leakage issues in the high-frequency band.

4.3. Model Applicability and Error Mechanism Analysis for Photonic Packaging Applications

To verify practical applicability in photonic-system packaging, a laser controller enclosure used in electro-optical instrumentation is selected for validation, as shown in Figure 9. The enclosure integrates a hexagonal honeycomb vent waveguide, representing a typical thermal-management interface in photonic hardware.

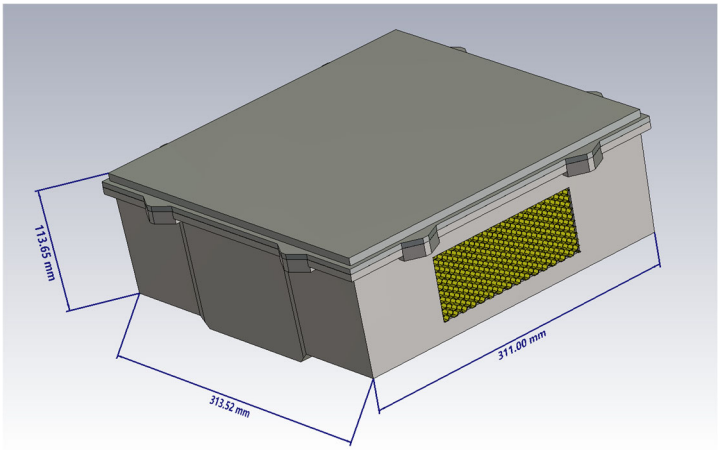


Figure 9. Laser controller enclosure equipped with a honeycomb waveguide.

The enclosure dimensions are 311 × 313.52 × 113.65 (mm) (L × W × H), while the honeycomb panel parameters are: a = 3 mm, L = 25 mm, and d = 3.5 mm. These parameters are kept identical in the analytical models and CST full-wave simulation to ensure a fair and consistent comparison.

The proposed model is specifically intended for laser controller enclosure applications. It is used to characterize aperture-induced leakage through the honeycomb-waveguide panel and to rapidly evaluate the shielding effectiveness of the controller housing during engineering design and optimization.

Based on the above configuration, Figure 10 compares the shielding effectiveness (SE) over 1–40 GHz obtained using the conventional analytical method, the proposed improved method, and CST simulation. The results include those from the proposed model (Line 1), traditional model (Line 2), and full-wave simulation (Line 3). In terms of the overall trend, all three curves exhibit a similar attenuation tendency at low frequencies, while they gradually diverge in the mid and high-frequency ranges. In particular, near and beyond the cutoff region, the conventional model overestimates SE, whereas the improved model shows significantly better agreement with the full-wave results.

As shown in Figure 10, the proposed improved model outperforms the conventional model across the entire frequency range, with especially notable improvement in the mid- to high-frequency band where it matches the simulation results more closely. The conventional model, based on ideal waveguide cutoff and additional loss terms, can capture the general attenuation trend. However, its assumptions—independent propagation in each aperture, ideal conducting boundaries, and weak array coupling—gradually break down at high frequencies, leading to a systematic overestimation of shielding performance.

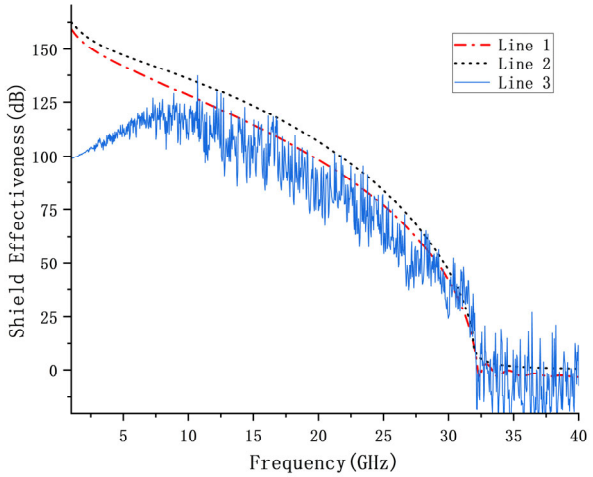


Figure 10. Shielding effectiveness in a motor controller enclosure.

In contrast, the proposed model introduces aperture-coupling correction and wall-loss correction within the conventional framework, enabling it to characterize enhanced energy leakage mechanisms under high-frequency conditions. As a result, it maintains good predictive capability near and beyond cutoff. These findings indicate that the new model not only preserves the advantages of analytical methods—high computational efficiency and strong parameter interpretability—but also significantly improves prediction reliability in engineering-critical frequency bands, making it suitable for rapid design and optimization of honeycomb ventilation structures.

Based on the observed parametric trends, a summarized design guideline for robust EMC packaging of photonic enclosures is proposed:

(1) Low-Frequency Cutoff Region: To enhance SE against low-frequency interference, increasing the waveguide length (L) yields a more dominant, linear improvement in exponential attenuation compared to narrowing the aperture.
(2) High-Frequency Resonance Region: To suppress high-frequency leakage, minimizing the aperture size (a) is required to push the dominant resonant peaks out of the critical operational band.
(3) Coupling Trade-off: While a thinner wall (d) reduces weight and aerodynamic resistance, it also intensifies inter-aperture coupling. Thus, a balanced cell density must be maintained to avoid excessive SE degradation from near-field overlapping.

4.4. Further Discussion

It should be noted that at low frequencies (e.g., below 10 GHz), some discrepancy remains between the improved model and full-wave simulation. This does not invalidate the model; the discrepancy mainly arises from two factors. First, the analytical model focuses on transmission through the honeycomb apertures themselves. In contrast, the simulation includes system-level effects such as finite enclosure size, edge diffraction, and cavity modes. These effects become more pronounced under long-wavelength (low-frequency) conditions. Second, practical simulations/structures may contain additional coupling paths outside the apertures (e.g., structural transitions and current return through gaps), and their influence is relatively stronger at low frequencies.

In other words, the low-frequency discrepancy essentially reflects a modeling-level difference between a “system-level full-structure response” and an “aperture-dominated analytical model.” It does not indicate insufficient physical significance of the proposed correction terms. Since the core improvements of this work target high-frequency aperture coupling and wall-dissipation mechanisms, the model shows more prominent accuracy

advantages in the 10–40 GHz band, which is also the more critical frequency range for engineering design.

While the proposed model enables rapid SE evaluation for photonic packaging, it inherently assumes ideal periodicity, neglecting finite edge diffractions and practical structural discontinuities (e.g., imperfect galvanic contacts and manufacturing tolerances). These non-ideal factors typically introduce additional leakage paths in real-world applications, presenting a crucial direction for future compensative optimizations. Furthermore, although formulated for macroscopic metallic honeycombs, our geometric cutoff framework shares a fundamental physical synergy with emerging nano-engineered porous materials [21,22] and terahertz wave suppression structures [23]. By integrating with effective medium theories, this baseline model holds the potential to scale down and predict the shielding performance of advanced microscopic hybrid conductive films in future studies.

5. Conclusions

In response to the limitations of traditional analytical models in forecasting the shielding effectiveness of high-density, high-frequency honeycomb waveguides, this research developed an enhanced semi-analytical model grounded in the transmission matrix method. By integrating frequency-dependent complex surface impedance and a mutual coupling factor derived from dipole array theory, the model effectively rectifies the previously overlooked wall ohmic losses and inter-aperture near-field interference, thereby effectively uncovering the mechanism of "virtual leakage channels" that deteriorate high-frequency performance. Verified through CST full-wave simulations, the proposed model improves prediction accuracy, especially in capturing attenuation trends near the cutoff frequency, while sustaining millisecond-scale computational efficiency. Although additional refinement is required to fully replicate sharp resonance drops and expand material applicability, this study effectively narrows the gap between simplified theories and complex numerical simulations, offering a physically robust and practical tool for optimizing photonic enclosure designs in terms of electromagnetic compatibility.

Author Contributions: Conceptualization, S.Z. and P.X.; methodology, S.Z. and P.X.; software, S.Z. and Z.T.; validation, S.Z., Y.H. and P.X.; formal analysis, S.Z. and P.X.; investigation, S.Z., Y.H. and Z.T.; resources, W.H.; data curation, S.Z. and Y.H.; writing—original draft preparation, S.Z.; writing—review and editing, S.Z., Y.H., F.L. and P.X.; visualization, S.Z. and Z.T.; supervision, Y.H. and W.H.; project administration, F.L.; funding acquisition, F.L. All authors have read and agreed to the published version of the manuscript.

Funding: This research was funded by the Central Leading Local Science and Technology Development Fund of Hunan Province, Grant number 2024ZYT007.

Data Availability Statement: All data generated or analyzed during this study are included in this published article.

Conflicts of Interest: The author Shaoqian Zhang, Yuanxin Huang, Wei He and Fuwei Li were employed by the Changsha Institute of Mining Research Co., Ltd. The author Fuwei Li was employed by the Minmetals National Innovation Center Technology (Hunan) Co., Ltd. All authors declare that the research was conducted in the absence of any commercial or financial relationships that could be construed as a potential conflict of interest.

References

1. Alarcon, W.A.; Engin, A.E.; Ndip, I.; Lang, K.-D. EBG Common-Mode Filter Design Using Uncoupled Coplanar Waveguide to Microstrip Transitions. *IEEE Lett. Electromagn. Compat. Pract. Appl.* **2020**, *2*, 81–84. [CrossRef]
2. Mao, H.; Wang, J.; Yu, K.; Zhu, Z. TM and TE propagating modes of photonic crystal waveguide based on honeycomb lattices. *Appl. Opt.* **2010**, *49*, 6597–6601. [CrossRef] [PubMed]

3. Lv, Q.; Peng, Z.; Pei, H.; Zhang, X.; Chen, Y.; Zhang, H.; Zhu, X. 3D printing of periodic porous metamaterials for tunable electromagnetic shielding across broad frequencies. *Nano-Micro Lett.* **2024**, *16*, 279. [CrossRef]
4. Bauer, S.; Renhart, W.; Bíroò, O.; Türk, C.; Maier, C.; Winkler, G.; Deutschmann, B. Investigation of SPICE Models for Overvoltage Protection Devices with Respect to Fast Transients. *IEEE Lett. Electromagn. Compat. Pract. Appl.* **2019**, *1*, 20–25. [CrossRef]
5. Chen, H.; Chen, H.; Xiu, X.; Xue, Q.; Che, W.; Chen, H.; Chen, H.D.; Xiu, X.; Xue, Q.; Che, W. Transparent FSS on Glass Window for Signal Selection of 5G Millimeter-Wave Communication. *IEEE Antennas Wirel. Propag. Lett.* **2021**, *20*, 2319–2323. [CrossRef]
6. Moser, J.R. Low-frequency low-impedance electromagnetic shielding. *IEEE Trans. Electromagn. Compat.* **2002**, *30*, 202–210. [CrossRef]
7. Koraqi, L.; Radhakrishnan, P.; Mora, A.C.; Claeys, T.; Catrysse, J.; Pissoort, D. Limitations of Schelkunoff's Model for Near-Field Shielding in the Two-Parallel Loops Configuration. In Proceedings of the 2025 International Symposium on Electromagnetic Compatibility–EMC Europe, Paris, France, 1–5 September 2025.
8. Afsari, A.; Abbosh, A.M.; Rahmat-Samii, Y. Adaptive Beamforming by Compact Arrays Using Evolutionary Optimization of Schelkunoff Polynomials. *IEEE Trans. Antennas Propag.* **2022**, *70*, 4485–4497. [CrossRef]
9. Ma, Z.; Ma, Z.; Lai, Y.; Lai, Y.; Huang, Q.; Huang, Q.; Yang, Y.; Yang, Y.; Wang, S.; Wang, S. Investigation and Mitigation of Radiated EMI due to Near-field Coupling in a High-density Active-clamp Flyback Power Adapter. In Proceedings of the 2023 IEEE Energy Conversion Congress and Exposition (ECCE), Nashville, TN, USA, 29 October–2 November 2023.
10. Zhang, Y.; Wu, X.; You, C. Fast Near-Field Beam Training for Extremely Large-Scale Array. *arXiv* **2022**, arXiv:2209.14798v1. [CrossRef]
11. Teng, S.; Tan, Y.; Cheng, C. Quasi-Talbot effect of the high-density grating in near field. *J. Opt. Soc. Am. A* **2008**, *25*, 2945–2951. [CrossRef] [PubMed]
12. Liu, Y.; Ouyang, C.; Wang, Z.; Xu, J.; Mu, X.; Swindlehurst, A.L. Near-field communications: A comprehensive survey. *IEEE Commun. Surv. Tutor.* **2024**. [CrossRef]
13. Gong, Y.; Karimi, M.; Le-Ngoc, T. Near-Field Nulling Control Beamfocusing Optimization for Multi-user Interference Suppression. *IEEE Open J. Commun. Soc.* **2025**, *6*, 1727–1746. [CrossRef]
14. Bingle, M.; Davidson, D.B.; Cloete, J.H. Scattering and absorption by thin metal wires in rectangular waveguide-FDTD simulation and physical experiments. *IEEE Trans. Microw. Theory Tech.* **2002**, *50*, 1621–1627. [CrossRef]
15. Albani, M.; Mazzinghi, A.; Freni, A. Rigorous MoM analysis of finite conductivity effects in RLSA antennas. *IEEE Trans. Antennas Propag.* **2011**, *59*, 4023–4032. [CrossRef]
16. Liu, Y.; Guo, Y.; Li, C.; Ye, X.; Kim, D. Surface Roughness Effect From Different Surfaces of Microstrip Lines and Reference Plane. *IEEE Lett. Electromagn. Compat. Pract. Appl.* **2023**, *5*, 92–96. [CrossRef]
17. Wang, Y.; Wu, X.; Yan, Y.; Wan, J.; Mo, J.; Jiang, Y.; Yu, X. Coplanar Discontinuous Transmission Line Feed for Phase Gradient Metasurface Antenna. *Int. J. Antennas Propag.* **2022**. [CrossRef]
18. Peng, X.; Qiu, W.; Wang, J.; Ma, L. A Novel Temporal Two-Grid Compact Finite Difference Scheme for the Viscous Burgers' Equation. *Adv. Appl. Math. Mech.* **2024**, *16*, 1358–1380. [CrossRef]
19. Pannipitiya, A.; Rukhlenko, I.D.; Premaratne, M.; Hattori, H.; Agrawal, G. Improved transmission model for metal-dielectric-metal plasmonic waveguides with stub structure. *Opt. Express* **2010**, *18*, 6191–6204. [CrossRef]
20. Meschi Amoli, B.; Hu, A.; Zhou, N.; Zhao, B. Recent progresses on hybrid micro–nano filler systems for electrically conductive adhesives (ECAs) applications. *J. Mater. Sci. Mater. Electron.* **2015**, *26*, 4730–4745. [CrossRef]
21. Kim, P.; Park, C.-H. The electronic structure and intervalley coupling of artificial and genuine graphene superlattices. *Nano Res.* **2016**, *9*, 1101–1115. [CrossRef]
22. Ma, L.; Lu, Z.; Tan, J.; Liu, J.; Ding, X.; Black, N.; Li, T.; Gallop, J.; Hao, L. Transparent Conducting Graphene Hybrid Films To Improve Electromagnetic Interference (EMI) Shielding Performance of Graphene. *ACS Appl. Mater. Interfaces* **2017**, *9*, 34221–34229. [CrossRef] [PubMed]
23. Rouhi, N.; Capdevila, S.; Jain, D.; Zand, K.; Wang, Y.Y.; Brown, E.; Jofre, L. Terahertz Graphene Optics. *Nano Res.* **2012**, *5*, 667–678. [CrossRef]

Disclaimer/Publisher's Note: The statements, opinions and data contained in all publications are solely those of the individual author(s) and contributor(s) and not of MDPI and/or the editor(s). MDPI and/or the editor(s) disclaim responsibility for any injury to people or property resulting from any ideas, methods, instructions or products referred to in the content.